Progress In Electromagnetics Research, Vol. 174, 33–42, 2022

TDFA-Band Silicon Optical Variable Attenuator

Maoliang Wei[1, 4], Hui Ma[1], Chunlei Sun[2, 3], Chuyu Zhong[1], Yuting Ye[2, 3], Peng Zhang[4], Ruonan Liu[4], Junying Li[1], Lan Li[2, 3], Bo Tang[4, *], and Hongtao Lin[1, *]

Abstract—TDFA-band (2-μm waveband) has been considered as a promising optical window for the next generation of optical communication and computing. Absorption modulation, one of the fundamental reconfigurable manipulations, is essential for large scale photonic integrated circuits. However, few efforts have been involved in exploring absorption modulation at TDFA-band. In this work, variable optical attenuators (VOAs) for TDFA-band wavelengths were designed and fabricated based on a silicon-on-insulator (SOI) platform. By embedding a short PIN junction length of 200 μm into the waveguide, the fabricated VOA exhibits a high modulation depth of 40.49 dB at 2.2 V and has a fast response time (10 ns) induced by the plasma dispersion effect. Combining the Fabry-Perot cavity effect and plasma dispersion effect of silicon, the attenuator could achieve a maximum attenuation of more than 50 dB. These results promote the 2-μm waveband silicon photonic integration and are expected to the future use of photonic attenuators in crosstalk suppression, optical modulation, and optical channel equalization.

1. INTRODUCTION

As data-intensive communication and computing applications develop dramatically, present optical techniques face challenges in the rapidly increasing bandwidth demand. Thanks to the availability of low-loss low-latency hollow-core photonic bandgap fibers (HC-PBGF) [1] and Thulium-doped fiber amplifiers (TDFAs) [2], the TDFA-band (2-μm waveband) wavelength region is now emerging as a potential new telecom waveband to expand the communication capacity [3, 4]. In recent years, many essential devices at 2-μm waveband have been demonstrated on germanium platforms [5–8], chalcogenide platforms [9–11], and III-V semiconductor platforms [12–14]. Especially, the silicon-on-insulator (SOI) platforms had attracted a lot of interest, due to their advantages of strong mode confinement and well-established complementary-metal-oxide-semiconductor (CMOS) fabrication processes [15–22]. However, the investigations of 2-μm integrated photonics circuits are still in infancy state. Many efforts are needed to design, fabricate, and characterize those missing integrated components.

Similar to metamaterial absorbers operating at terahertz and gigahertz [23, 24], variable optical attenuators (VOAs) can tune the intensity of light. VOAs are essential components for many applications in optic communications, especially for signal equalization in upstream optical packets. The attenuator could also enable a scalar multiply operation [25, 26]. It could be scaled up to build a photonic tensor core with the assistance of an on-chip frequency comb, which is essential for realizing an on-chip non-von Neumann microprocessor [27]. They would also play a significant role in emerging

Received 13 January 2022, Accepted 8 April 2022, Scheduled 30 April 2022

* Corresponding author: Hongtao Lin (hometown@zju.edu.cn), Bo Tang (tangbo@ime.ac.cn).

[1] State Key Laboratory of Modern Optical Instrumentation, College of Information Science and Electronic Engineering, Zhejiang University, Hangzhou 310027, China. [2] Key Laboratory of 3D Micro/Nano Fabrication and Characterization of Zhejiang Province, School of Engineering, Westlake University, Hangzhou, Zhejiang 310024, China. [3] Institute of Advanced Technology, Westlake Institute for Advanced Study, Hangzhou, Zhejiang 310024, China. [4] Institute of Microelectronics of the Chinese Academy of Sciences, Beijing 100029, China.

large-scale optical systems such as optical interconnect processors [28–30], memories [31], optical neural networks [32–36], and optical phased arrays [37, 38]. Different kinds of silicon VOAs operated in the O/C band have been intensively studied [6, 39, 40], but few works were conducted for VOAs working at the TDFA-band.

Optical attenuation for silicon VOAs can be implemented by changing the complex refractive index of the waveguide mode, i.e., by changing the real part of the refractive index (refraction) or/and the imaginary part of the refractive index (absorption). Interferometric waveguide configurations, such as Mach-Zehnder Interferometers (MZIs) or resonators, are commonly adopted for refraction-tuning types of silicon VOAs. Phase shift tuning in integrated optical paths in these devices usually relies on the electro-optical (EO) or thermo-optic (TO) effect in silicon photonics. EO phase shifter consisting of a silicon PN junction can modulate light at a speed of tens of GHz. However, the size of devices is usually in the millimeters range due to the small refractive index change of carrier depletion in silicon [41]. Thermo-optical silicon VOAs could be compact with high attenuation ratio, but their response time ($\sim$ μs to ms range) is slow [42–44]. Besides, the interferometric configuration results in undesired wavelength dependence of attenuation in refractive-tuning types of silicon VOAs, which is unfavored for large-scale photonic systems. Utilizing the carrier injection effect of silicon, silicon VOAs with broadband operation window and moderate modulation speed (about 10 ns) can be realized. This is highly desired for the wavelength division multiplexing passive optical networks (WDM-PONs) and other emerging applications. Besides, the attenuation coefficient at 2 μm induced by the injected carrier could be around 1.7 times greater than that at 1.55 μm [45]. As a result, it is possible to realize more compact and energy-efficient absorptive VOAs at 2 μm.

In this paper, we demonstrate high-speed TDFA-band VOAs based on a 220-nm SOI platform utilizing carrier injection and free-carrier absorption effect. By embedding the PIN junction into the waveguide, we obtain high carrier-injection efficiency and high-speed intensity modulation. The insertion loss of the attenuator without bias voltage could be neglected, and the minimum attenuation is as high as 40.49 dB for a 200-μm-long VOA with a bias voltage of 2.2 V. By taking advantage of the Fabry-Perot effect, the maximum attenuation could achieve more than 50 dB. Benefiting from the compact size of the VOA, the device demonstrates a fast response time (10%–90% rise time) of 10 ns.

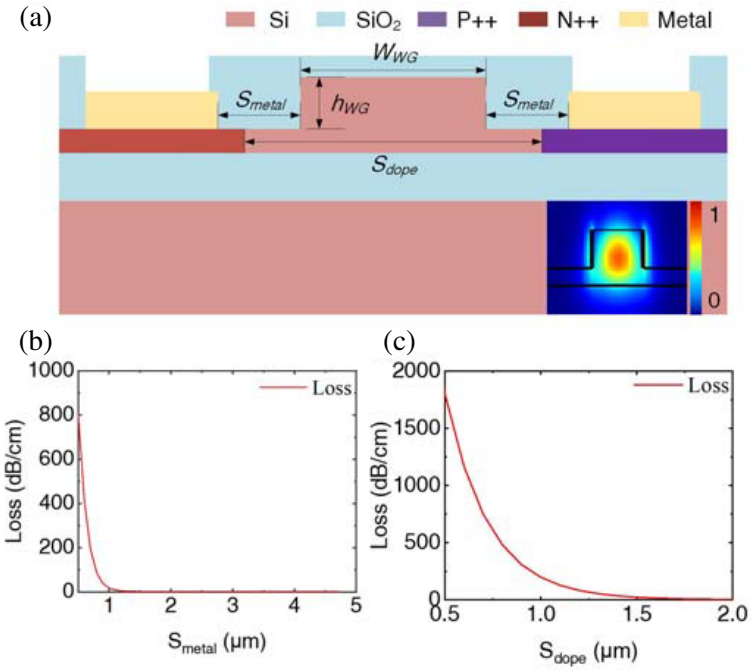

Figure 1. (a) Cross-sectional diagram of the VOA, the inset is the optical mode of the waveguide. (b) The simulated loss of the waveguide varied with the distance between the waveguide core and metal contacts. (c) The simulated optical loss changed with the variation of the doping distance.

2. OPERATION PRINCIPLE AND SIMULATION

Figure 1(a) shows the cross-sectional diagram of the waveguide with a width (W_{WG}) of 600 nm and a ridge height (h_{WG}) of 150 nm. In this work, we set the distance between the waveguide core and metal pads (S_{metal}) to 3.7 µm, which is sufficient to avoid additional losses introduced by the metal absorption (Figure 1(b)). The sides of the core waveguide are symmetric p-type and n-type doped silicon, respectively. The targeted doping concentrations are 2.472×10^{20} and $2.781 \times 10^{20}\,\mathrm{cm}^{-3}$ for the heavy p-type and n-type regions, respectively. The loss of the waveguide is decreased with the increase of the distance between p-type and n-type doping (S_{dope}). As shown in Figure 1(c), the loss induced by doped silicon is negligible when the distance (S_{dope}) is larger than 1.5 µm. In our design, the S_{dope} is set to 1.5 µm.

To estimate the electrical and optical performance of the PIN junction, a 2D simulation in Lumerical Device was conducted by solving the distribution of carriers. The electron concentration distributions of the ridge waveguide under different biases are shown in Figure 2(a). The PIN attenuators were operated in a forward bias mode, where the number of electrons transported and the current increases exponentially with the increasing applied voltage. Due to the plasma dispersion effect, the refractive index of the silicon decreases while the absorption increases with the injection of carriers in the PIN junction [46]. The simulated waveguide's effective refractive index and propagation loss in the PIN junction region at 2025 nm are illustrated in Figure 2(b). The attenuation of the 200-µm-long PIN junction waveguide could be designed to achieve 36.24 dB at a bias of 2.2 V. By utilizing the Fabry-Perot effect [47], a higher extinction ratio could be realized at 2 µm waveband.

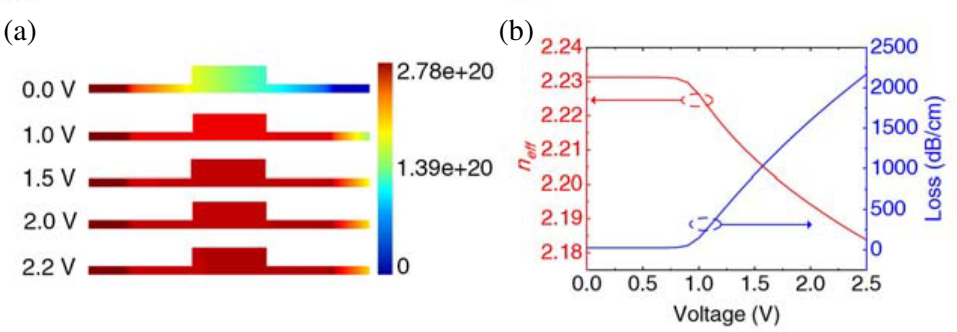

Figure 2. (a) Electron concentration distribution of a PIN junction at 0 V, 1.0 V, 1.5 V, 2.0 V, and 2.2 V. (b) The effective refractive index and propagation loss of a PIN junction at different forward biases at the wavelength of 2025 nm.

3. DEVICE FABRICATION

Figure 3(a) illustrates the fabrication process of the VOA. The device is based on the silicon on insulator (SOI) platform. Before fabricating the metal contacts, the patterning and doping of the waveguides were conducted in the Institute of Microelectronics of the Chinese Academy of Sciences (IMECAS) in a customized multi-process wafer (MPW) run. The process started from an SOI wafer with a 220 nm-thick top silicon layer. The pattern of the waveguide and the doped silicon regions was defined by deep ultra-violet (DUV) photolithography.

Firstly, 150-nm-thick silicon was etched by the inductive coupling plasma (ICP) etching process. We have characterized the low-loss waveguide, and the propagation loss of the 150 nm ridge waveguide was 1.62 dB/cm [18]. Then, boron ions with a concentration of $1.7 \times 10^{20}\,\mathrm{cm}^{-3}$ and phosphorous ions with a concentration of $1.7 \times 10^{20}\,\mathrm{cm}^{-3}$ were implanted subsequently to form the heavy p-type and n-type regions. The doping concentrations of p-type and n-type doping were $2.472 \times 10^{20}\,\mathrm{cm}^{-3}$, $2.781 \times 10^{20}\,\mathrm{cm}^{-3}$, respectively, measured by Hall bar devices. Afterward, the metal contacts were patterned by electron-beam lithography (EBL, Raith Voyager) with positive-tone resist (ARP 6200.13). The 5-nm-thick Ti/100-nm-thick Au metal contacts were fabricated by electron beam evaporation (Ei-

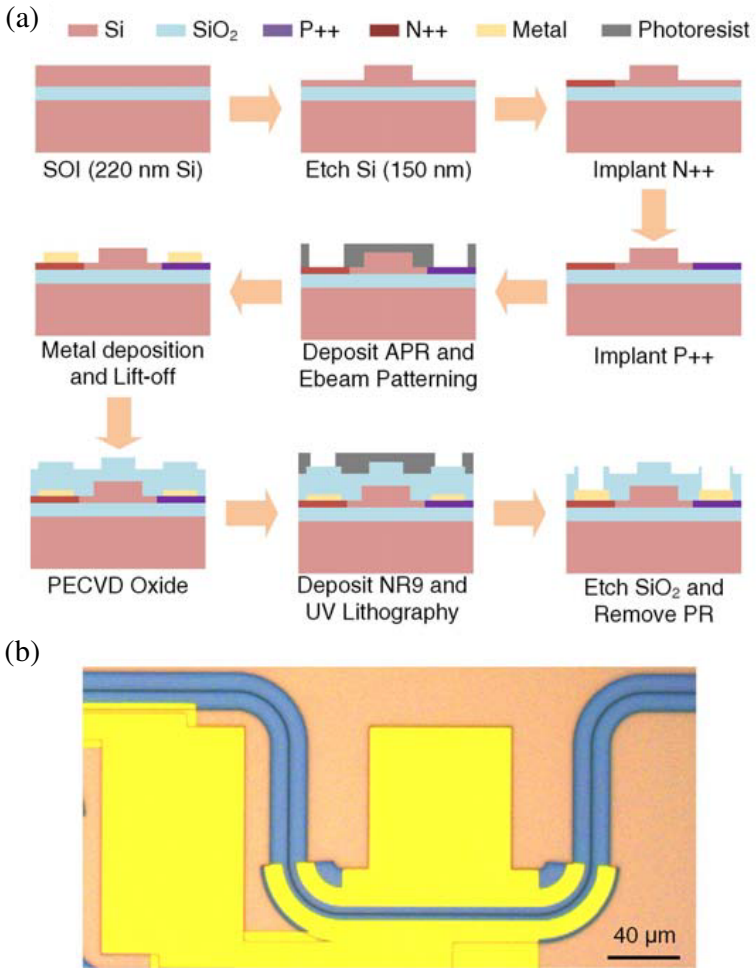

Figure 3. (a) The fabrication flow chart of the VOA. (b) The micrograph of the fabricated VOA.

5Z) followed by a lift-off process. The device was then covered with 1-μm thick silicon dioxide by plasma-enhanced chemical vapor deposition (PECVD, DISCOVERY-635), and electrode windows were opened via hydrofluoric acid wet etching. Figure 3(b) is a micrograph of a fabricated PIN junction-based photonic attenuator. The device consists of a 200-μm long PIN junction in a rib waveguide. The bending radius of the partially etched waveguide was set to 30 μm to get rid of the bending loss of the waveguide. The VOA could actively tune the transmittance of light in the photonic integrated circuits.

4. RESULTS AND DISCUSSIONS

A 2 μm tunable laser transmission measurement system and a fiber coupling system were set up to characterize the fabricated PIN attenuator. Details of the setup were described in our previous work [19]. A source meter (Keithly 2450) was used to apply the forward bias voltage while recording the current going through the PIN junctions. A commercial RF probe (GGB 40A-GS-150-DP) was used to apply the electrical signal to the device under test (DUT). A photodetector measured the light passing through the attenuators. As shown in Figure 4(a), the current of our VOA increased sharply at a forward bias greater than 0.8 V, while the output power simultaneously decreased.

The reduction of normalized transmission at 2025 nm (Figure 4(a)) is due to the carrier injection into the waveguide core. By applying a voltage of 2.2 V to the attenuator, the attenuation reached 40.49 dB, and the corresponding power consumption was 223.50 mW. The slight difference in extinction ratio results from the unstable contact between the radio frequency (RF) probe and the metal contacts.

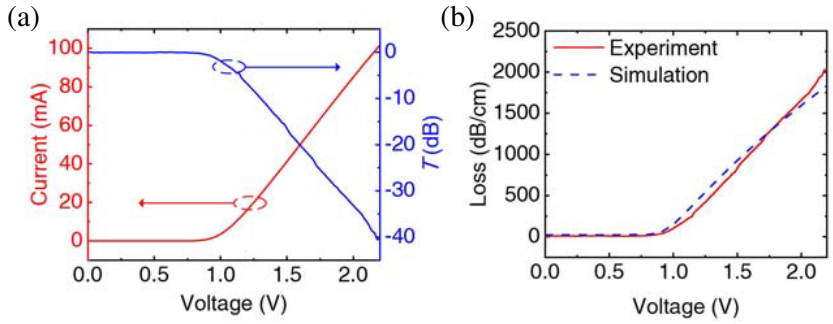

Figure 4. (a) The measured current and transmission at different forward biases at the wavelength of 2025 nm. (b) The simulated and measured attenuation coefficient of the PIN-integrated photonic attenuator at 2025 nm.

The attenuation coefficient α is given by

$$\alpha = \frac{T_0 - T}{l} \tag{1}$$

where T_0 and T are the transmission at 0 V and varied bias voltages, and l is the length of the photonic attenuator (200 µm in our proposed attenuator). As shown in Figure 4(b), the measured attenuation coefficient agrees well with the simulated ones at a voltage less than 1.6 V. When the forward bias is larger than 1.6 V, the measured attenuation coefficient is larger than the simulated one.

To analyze the discrepancy, we performed the measurements of transmission spectra of the attenuator under different bias voltages, which are shown in Figure 5. From the spectra, we observed interference peaks when the bias voltage was larger than 1.6 V. When the voltage is larger than 2 V, the performance of the attenuator is strongly wavelength-dependent, which would be attributed to the cavity-enhanced absorption. This is due to a non-ignorable mode mismatch at the interfaces between the doped and undoped waveguides. When a forward bias is applied to the VOA, the difference in refractive index between the PIN junction and the intrinsic silicon waveguide causes Fresnel reflections. Thus, a Fabry-Perot cavity is formed and leads to spectral interference patterns. This is also the reason for the discrepancy of the simulated and measured attenuation coefficients at 2025 nm for the attenuator. By utilizing cavity-enhanced optical attenuation, a high attenuation of 50 dB, as well as low power consumption, could be achieved at the 2 µm waveband based on an attenuator with a shorter PIN length (Figure 5).

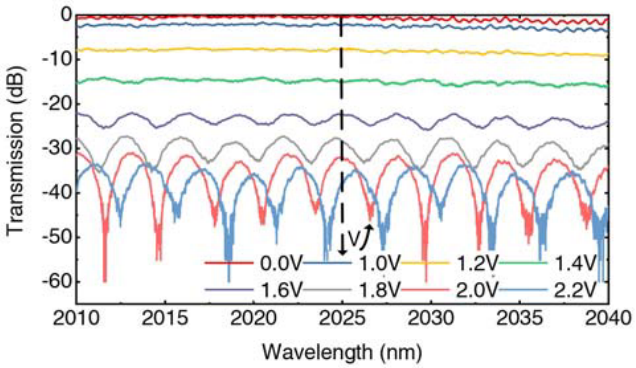

Figure 5. The measured transmission spectra of the VOA at different bias voltages.

To evaluate the modulation speed of the VOA, a 10 MHz square-wave signal generated by an arbitrary waveform generator (AWG, Siglent SDG6032X-E) was applied through the metal contacts of the attenuator. The optical response was collected by a high-speed photodetector, amplified by a

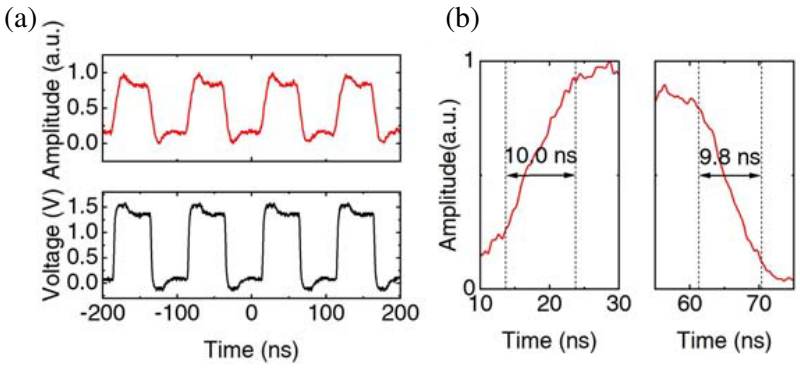

Figure 6. (a) The temporal response of the VOA and the corresponding square-wave signal generated by AWG. (b) The enlarged temporal response and corresponding rising and falling time.

pulse forming amplifier (PFA), and then sampled by a real-time oscilloscope (Siglent SDS5104X). At the wavelength of 2025 nm, the extinction ratio for the on-off states was measured to be 9.93 dB when a square wave with a peak voltage of 1.3 V was applied. The 10%–90% rise and 90%–10% fall times were 10 ns and 9.8 ns, respectively, as shown in Figure 6. The corresponding 3 dB bandwidth can be estimated by

$$\text{Bandwidth} = \frac{0.35}{t_{\text{rise}}} \tag{2}$$

where t_{rise} is the rise time of the device. The bandwidth of the device was estimated to be 35 MHz.

Table 1. Performance comparison in different types of VOA.

Operation Principle [Ref.]	Wavelength (nm)	Device length (μm)	Insertion Loss (dB)	Maximum extinction ratio (dB)	Rise/Fall time τ	Year
Optoelectro-mechanical [39]	1550	45	0	36	∼ 1 ms	2018
Thermo-optical [40]	1550	200[1]	N/A	20	11.7 μs	2019
Thermo-optical (TiN heater) [42]	2000	100	2–3	30	15 μs	2019
Electro-optical (injection) of Ge [6]	∼ 2000[2]	250	N/A	∼ 23	N/A	2020
Electro-optical (depletion) [41]	1952	2000	10	22	< 19.4 ps	2021
Thermo-optical [19]	2005	100	1.13	17	3.49/3.46μs	2021
Electro-optical (injection) [This work]	2025	200	0	40.49	10/9.8 ns	2022

[1] The length of the metal heater

[2] 2-μm waveband

Although the modulation speed of this VOA is not comparable with the plasmonic hybrid waveguides or graphene hybrid waveguides, the low insertion loss, CMOS-compatibility of our proposed scheme is beneficial for 2-μm large-scale integrated systems. Moreover, by embedding a passive-circuit equalizer, the bandwidth of the VOA can be further improved [48].

We draw a direct comparison between our VOA and other attenuator modulation approaches operating at 1550-nm and 2-μm waveband in Table 1 considering the device length (the length of tuning region), insertion loss, maximum extinction ratio, rise/fall time, drive voltage, drive current, and year. The PIN-junction-embedded VOA in this work demonstrated a faster response time than that utilizing optoelectro-mechanical or thermo-optical effect. Meanwhile, an extinction ratio of 40.49 dB within a compact device length of 200 μm was demonstrated in this work. This VOA achieved a high extinction ratio and moderate modulation speed within a compact device length.

5. CONCLUSION

In conclusion, we designed and fabricated PIN-junction-based silicon VOAs at the TDFA band by utilizing plasma dispersion effect. The PIN-integrated VOA at the TDFA band exhibited a negligible insertion loss and a large modulation depth of 40.49 dB. Cavity-enhanced attenuation was observed for the first time to the best of our knowledge. The attenuators could achieve an attenuation of more than 50 dB due to the Fresnel reflection induced by a high concentration of injected carriers. The attenuator is much faster than conventional thermo-optic attenuators and could achieve both 10%–90% rise time and 90%–10% fall time less than ten nanoseconds. We believe that the absorption-modulation scheme proposed in this paper is a significant pavement for designing a reconfigurable photonic integrated circuit at the TDFA band.

FUNDING

This work was supported by the National Key Research and Development Program of China (Grant Number 2019YFB2203003), National Natural Science Foundation of China (Grant Numbers 91950204 and 61975179), Open Fund of the State Key Laboratory of Integrated Optoelectronics (Grant Number IOSKL2020KF05), and the Fundamental Research Funds for the Central Universities (Grant Number 2021QNA5007).

ACKNOWLEDGMENT

The authors would like to acknowledge the fabrication and simulation software (Lumerical) support from the Institute of Microelectronics of the Chinese Academy of Sciences, ZJU Micro-Nano Fabrication Center in Zhejiang University, and Westlake Center for Micro/Nano Fabrication in Westlake University.

AUTHOR CONTRIBUTIONS

L.H., B.T., and L.L. conceived the project. M.W., H.M., C.S., C.Z., Y.Y., P.Z., R.L., J.L., and B.T. fabricated these devices. M.W. performed optical and optoelectronic measurements. M.W., H.M., C.S., H.L., and B.T. analyzed the data and wrote the manuscript. All authors commented on the manuscript.

DISCLOSURES

The authors declare no conflicts of interest.

REFERENCES

1. Shen, W., J. Du, L. Sun, C. Wang, Y. Zhu, K. Xu, B. Chen, and Z. He, "Low-latency and high-speed hollow-core fiber optical interconnection at 2-micron waveband," *Journal of Lightwave Technology*, Vol. 38, No. 15, 3874–3882, 2020.

2. Li, Z., A. M. Heidt, J. M. O. Daniel, Y. Jung, S. U. Alam, and D. J. Richardson, "Thulium-doped fiber amplifier for optical communications at 2 μm," *Optics Express*, Vol. 21, No. 8, 9289–9297, 2013.
3. Soref, R., "Mid-infrared photonics in silicon and germanium," *Nature Photonics*, Vol. 4, No. 8, 495–497, 2010.
4. Soref, R., "Enabling 2 μm communications," *Nature Photonics*, Vol. 9, No. 6, 358–359, 2015.
5. Takenaka, M., Z. Zhao, C. P. Ho, T. Fujigaki, K. Toprasertpong, and S. Takagi, "Germanium mid-infrared integrated photonics on geoi platform," *Conference on Lasers and Electro-Optics*, Optical Society of America, San Jose, California, 2021.
6. Zhao, Z., C. P. Ho, Q. Li, Z. Lin, K. Toprasertpong, S. Takagi, and M. Takenaka, "Efficient mid-infrared germanium variable optical attenuator fabricated by spin-on-glass doping," *Journal of Lightwave Technology*, Vol. 38, No. 17, 4808–4816, 2020.
7. Kang, J., M. Takenaka, and S. Takagi, "Novel Ge waveguide platform on Ge-on-insulator wafer for mid-infrared photonic integrated circuits," *Optics Express*, Vol. 24, No. 11, 11855–11864, 2016.
8. Li, X., J. X. B. Sia, W. Wang, Z. Qiao, X. Guo, G. I. Ng, Y. Zhang, Z. Niu, C. Tong, H. Wang, and C. Liu, "Phase noise reduction of a 2 μm passively mode-locked laser through hybrid III-V/silicon integration," *Optica*, Vol. 8, No. 6, 855–860, 2021.
9. Shen, W., P. Zeng, Z. Yang, D. Xia, J. Du, B. Zhang, K. Xu, Z. He, and Z. Li, "Chalcogenide glass photonic integration for improved 2 μm optical interconnection," *Photonics Research*, Vol. 8, No. 9, 1484–1490, 2020.
10. Lin, H., Y. Song, Y. Huang, D. Kita, S. Deckoff-Jones, K. Wang, L. Li, J. Li, H. Zheng, Z. Luo, H. Wang, S. Novak, A. Yadav, C.-C. Huang, R.-J. Shiue, D. Englund, T. Gu, D. Hewak, K. Richardson, J. Kong, and J. Hu, "Chalcogenide glass-on-graphene photonics," *Nature Photonics*, Vol. 11, No. 12, 798–805, 2017.
11. Han, Z., P. Lin, V. Singh, L. Kimerling, J. Hu, K. Richardson, A. Agarwal, and D. T. H. Tan, "On-chip mid-infrared gas detection using chalcogenide glass waveguide," *Applied Physics Letters*, Vol. 108, No. 14, 141106, 2016.
12. Sadiq, M. U., H. Zhang, J.O. Callaghan, B. Roycroft, N. Kavanagh, K. Thomas, A. Gocalinska, Y. Chen, T. Bradley, J.R. Hayes, Z. Li, S. U. Alam, F. Poletti, M. N. Petrovich, D. J. Richardson, E. Pelucchi, P. O. Brien, F. H. Peters, F. Gunning, and B. Corbett, "40 Gb/s WDM transmission over 1.15-km HC-PBGF using an InP-based Mach-Zehnder modulator at 2 μm," *Journal of Lightwave Technology*, Vol. 34, No. 8, 1706–1711, 2016.
13. Yang, C.-A., S.-W. Xie, Y. Zhang, J.-M. Shang, S.-S. Huang, Y. Yuan, F.-H. Shao, Y. Zhang, Y.-Q. Xu, and Z.-C. Niu, "High-power, high-spectral-purity GaSb-based laterally coupled distributed feedback lasers with metal gratings emitting at 2 μm," *Applied Physics Letters*, Vol. 114, No. 1, 021102, 2019.
14. Wang, R., S. Sprengel, G. Boehm, R. Baets, M.-C. Amann, and G. Roelkens, "Broad wavelength coverage 2.3 μm III-V-on-silicon DFB laser array," *Optica*, Vol. 4, No. 8, 972–975, 2017.
15. Ackert, J. J., D. J. Thomson, L. Shen, A. C. Peacock, P. E. Jessop, G. T. Reed, G. Z. Mashanovich, and A. P. Knights, "High-speed detection at two micrometres with monolithic silicon photodiodes," *Nature Photonics*, Vol. 9, No. 6, 393–396, 2015.
16. Cao, W., D. Hagan, D.J. Thomson, M. Nedeljkovic, C. G. Littlejohns, A. Knights, S.-U. Alam, J. Wang, F. Gardes, W. Zhang, S. Liu, K. Li, M. S. Rouifed, G. Xin, W. Wang, H. Wang, G. T. Reed, and G. Z. Mashanovich, "High-speed silicon modulators for the 2 μm wavelength band," *Optica*, Vol. 5, No. 9, 1055–1062, 2018.
17. Hattasan, N., B. Kuyken, F. Leo, E. M. P. Ryckeboer, D. Vermeulen, and G. Roelkens, "High-efficiency SOI fiber-to-chip grating couplers and low-loss waveguides for the short-wave infrared," *IEEE Photonics Technology Letters*, Vol. 24, No. 17, 1536–1538, 2012.
18. Ma, H., H. Yang, B. Tang, M. Wei, J. Li, J. Wu, P. Zhang, C. Sun, L. Li, and H. Lin, "Passive devices at 2 μm wavelength on 200 mm CMOS-compatible silicon photonics platform [Invited]," *Chinese Optics Letters*, Vol. 19, No. 7, 071301, 2021.

19. Zhong, C., H. Ma, C. Sun, M. Wei, Y. Ye, B. Tang, P. Zhang, R. Liu, J. Li, L. Li, and H. Lin, "Fast thermo-optical modulators with doped-silicon heaters operating at 2 µm," *Optics Express*, Vol. 29, No. 15, 23508–23516, 2021.
20. Wang, Z., Y. Liu, Z. Wang, Y. Liu, J. Du, Q. Song, and K. Xu, "Ultra-broadband 3 dB power splitter from 1.55 to 2 µm wave band," *Optics Letters*, Vol. 46, No. 17, 4232–4235, 2021.
21. Guo, J., J. Li, C. Liu, Y. Yin, W. Wang, Z. Ni, Z. Fu, H. Yu, Y. Xu, Y. Shi, Y. Ma, S. Gao, L. Tong, and D. Dai, "High-performance silicon-graphene hybrid plasmonic waveguide photodetectors beyond 1.55 µm," *Light: Science & Applications*, Vol. 9, No. 1, 29, 2020.
22. Duan, F., K. Chen, D. Chen, and Y. Yu, "Low-power and high-speed 2×2 thermo-optic MMI-MZI switch with suspended phase arms and heater-on-slab structure," *Optics Letters*, Vol. 46, No. 1, 234–237, 2021.
23. Jain, P., A. K. Singh, J.K. Pandey, S. Bansal, N. Sardana, S. Kumar, N. Gupta, and A. K. Singh, "An ultrathin compact polarization-sensitive triple-band microwave metamaterial absorber," *Journal of Electronic Materials*, Vol. 50, No. 3, 1506–1513, 2021.
24. Jain, P., A. K. Singh, J. K. Pandey, S. Garg, S. Bansal, M. Agarwal, S. Kumar, N. Sardana, N. Gupta, and A. K. Singh, "Ultra-thin metamaterial perfect absorbers for single-/dual-/multi-band microwave applications," *IET Microwaves, Antennas & Propagation*, Vol. 14, No. 5, 390–396, 2020.
25. Ros, C., N. Youngblood, Z. Cheng, M. Le Gallo, H. P. Pernice Wolfram, C. D. Wright, A. Sebastian, and H. Bhaskaran, "In-memory computing on a photonic platform," *Science Advances*, Vol. 5, No. 1, eaau5759, 2019.
26. Cheng, Z. G., C. Rios, W. H. P. Pernice, C. D. Wright, and H. Bhaskaran, "On-chip photonic synapse," *Science Advances*, Vol. 3, No. 9, e1700160, 2017.
27. Feldmann, J., N. Youngblood, M. Karpov, H. Gehring, X. Li, M. Stappers, M. Le Gallo, X. Fu, A. Lukashchuk, A. S. Raja, J. Liu, C. D. Wright, A. Sebastian, T. J. Kippenberg, W. H. P. Pernice, and H. Bhaskaran, "Parallel convolutional processing using an integrated photonic tensor core," *Nature*, Vol. 589, No. 7840, 52–58, 2021.
28. Sun, C., M. T. Wade, Y. Lee, J. S. Orcutt, L. Alloatti, M. S. Georgas, A. S. Waterman, J. M. Shainline, R. R. Avizienis, S. Lin, B. R. Moss, R. Kumar, F. Pavanello, A. H. Atabaki, H. M. Cook, A. J. Ou, J. C. Leu, Y. H. Chen, K. Asanovic, R. J. Ram, M. A. Popovic, and V. M. Stojanovic, "Single-chip microprocessor that communicates directly using light," *Nature*, Vol. 528, No. 7583, 534–538, 2015.
29. Zhang, W. and J. Yao, "A fully reconfigurable waveguide Bragg grating for programmable photonic signal processing," *Nature Communications*, Vol. 9, No. 1, 1396, 2018.
30. Zhang, W. and J. Yao, "Photonic integrated field-programmable disk array signal processor," *Nature Communications*, Vol. 11, No. 1, 406, 2020.
31. Feldmann, J., N. Youngblood, X. Li, C. D. Wright, H. Bhaskaran, and W. H. P. Pernice, "Integrated 256 cell photonic phase-change memory with 512-bit capacity," *IEEE Journal of Selected Topics in Quantum Electronics*, Vol. 26, No. 1, 1–7, 2020.
32. Shen, Y., N. C. Harris, S. Skirlo, M. Prabhu, T. Baehr-Jones, M. Hochberg, X. Sun, S. Zhao, H. Larochelle, D. Englund, and M. Soljačić, "Deep learning with coherent nanophotonic circuits," *Nature Photonics*, Vol. 11, No. 7, 441–446, 2017.
33. Feldmann, J., N. Youngblood, C. D. Wright, H. Bhaskaran, and W. H. P. Pernice, "All-optical spiking neurosynaptic networks with self-learning capabilities," *Nature*, Vol. 569, No. 7755, 208–214, 2019.
34. Wu, C., H. Yu, S. Lee, R. Peng, I. Takeuchi, and M. Li, "Programmable phase-change metasurfaces on waveguides for multimode photonic convolutional neural network," *Nature Communications*, Vol. 12, No. 1, 96, 2021.
35. Xu, S., J. Wang, H. Shu, Z. Zhang, S. Yi, B. Bai, X. Wang, J. Liu, and W. Zou, "Optical coherent dot-product chip for sophisticated deep learning regression," *Light: Science & Applications*, Vol. 10, No. 1, 221, 2021.

36. Xu, X., L. Zhu, W. Zhuang, D. Zhang, P. Yuan, and L. Lu, "Photoelectric hybrid convolution neural network with coherent nanophotonic circuits," *Optical Engineering*, Vol. 60, No. 11, 2021.
37. Kang, G., C.-H. Youn, K. Yu, H.-H. Park, S.-H. Kim, J.-B. You, D.-S. Lee, H. Yoon, Y.-G. Ha, J.-H. Kim, D.-E. Yoo, and D.-W. Lee, "Silicon-based optical phased array using electro-optic p-i-n phase shifters," *IEEE Photonics Technology Letters*, Vol. 31, No. 21, 1685–1688, 2019.
38. Miller, S. A., Y.-C. Chang, C. T. Phare, M.C. Shin, M. Zadka, S. P. Roberts, B. Stern, X. Ji, A. Mohanty, O. A. Jimenez Gordillo, U. D. Dave, and M. Lipson, "Large-scale optical phased array using a low-power multi-pass silicon photonic platform," *Optica*, Vol. 7, No. 1, 3–6, 2020.
39. Teodoro, G., S. Hamed, S. Tae Joon, H. Sangyoon, C.W. Ming, and Q. Niels, "Silicon photonic MEMS variable optical attenuator," *Proc. SPIE*, 2018.
40. El-Fiky, E., M. Jacques, A. Samani, L. H. Xu, M. G. Saber, and D. V. Plant, "C-band and O-band silicon photonic based low-power variable optical attenuators," *IEEE Photonics Journal*, Vol. 11, No. 4, 2019.
41. Wang, X., W. Shen, W. Li, Y. Liu, Y. Yao, J. Du, Q. Song, and K. Xu, "High-speed silicon photonic Mach-Zehnder modulator at 2 µm," *Photonics Research*, Vol. 9, No. 4, 535–540, 2021.
42. Shen, L., M. Huang, S. Zheng, L. Yang, X. Peng, X. Cao, S. Li, and J. Wang, "High-performance silicon 2×2 thermo-optic switch for the 2 µm wavelength band," *IEEE Photonics Journal*, Vol. 11, No. 4, 1–6, 2019.
43. Shen, W., J. Du, K. Xu, and Z. He, "On-chip selective dual-mode switch for 2-µm wavelength high-speed optical interconnection," *IEEE Photonics Technology Letters*, Vol. 33, No. 10, 483–486, 2021.
44. Dong, P., W. Qian, H. Liang, R. Shafiiha, D. Feng, G. Li, J. E. Cunningham, A. V. Krishnamoorthy, and M. Asghari, "Thermally tunable silicon racetrack resonators with ultralow tuning power," *Optics Express*, Vol. 18, No. 19, 20298–20304, 2010.
45. Nedeljkovic, M., R. Soref, and G. Z. Mashanovich, "Free-carrier electrorefraction and electroabsorption modulation predictions for silicon over the 1–14 µm infrared wavelength range," *IEEE Photonics Journal*, Vol. 3, No. 6, 1171–1180, 2011.
46. Reed, G. T., G. Mashanovich, F. Y. Gardes, and D. J. Thomson, "Silicon optical modulators," *Nature Photonics*, Vol. 4, No. 8, 518–526, 2010.
47. Thomson, D. J., L. Shen, J. J. Ackert, E. Huante-Ceron, A. P. Knights, M. Nedeljkovic, A. C. Peacock, and G. Z. Mashanovich, "Optical detection and modulation at 2 µm–2.5 µm in silicon," *Optics Express*, Vol. 22, No. 9, 10825–10830, 2014.
48. Baba, T., S. Akiyama, M. Imai, and T. Usuki, "25-Gb/s broadband silicon modulator with 0.31-V·cm $V_\pi L$ based on forward-biased PIN diodes embedded with passive equalizer," *Optics Express*, Vol. 23, No. 26, 32950–32960, 2015.